

On–off and proportional–integral controller for a morphing wing. Part 1: Actuation mechanism and control design

T L Grigorie¹, A V Popov¹, R M Botez^{1*}, M Mamou², and Y Mébarki²

¹École de Technologie Supérieure, Montréal, Québec, Canada

²National Research Council, Ottawa, Ontario, Canada

The manuscript was received on 27 August 2010 and was accepted after revision for publication on 4 April 2011.

DOI: 10.1177/0954410011408226

Abstract: The main objective of this research work is the development of an actuation control concept for a new morphing actuation mechanism made of smart materials, which is built from a shape memory alloy (SMA). Two lines of smart actuators were incorporated to a rectangular wing to modify the upper wing surface, made of a flexible skin, with the intention to move the laminar-to-turbulent transition point closer to the wing trailing edge.

After a brief introduction of the morphing wing system architecture and requirements, the actuation lines' design and instrumentation are presented. The integrated controller controls the SMA actuators via an electrical current supply, so that the transducer position can be used to eliminate the deviation between the required values for vertical displacements (corresponding to the optimized airfoils) and their physical values. The final configuration of the integrated controller is a combination of a bi-positional (on–off) controller and a PI (proportional–integral) controller, due to the two heating and cooling phases of the SMA wires' interconnection. This controller must behave like a switch between the cooling and the heating phases, situations where the output current is 0 A, or is controlled by a PI type law. The PI controller for the heating phase is optimally tuned using integral and surface minimum error criteria (Ziegler–Nichols). The controller is numerically tested on the linear identified system in terms of time response, Bode diagram, amplitude and phase stability margins, and root-locus.

Keywords: morphing wing, actuation mechanism, control design, numerical simulation, testing

1 INTRODUCTION

Pushed by the increasing requirements for more efficient flight technologies, the concept of aircraft wing morphing has undergone various forms of theoretical design, modelling, and experimental testing. A series of technologies that allow an aircraft to rapidly change its shape during flight have been developed [1, 2]. Interest in applying these new technologies in the aerospace industry has grown due mainly to the recent advances in the field of adaptive and

intelligent structures. These structures generally use smart materials and intelligent control systems. The aim of this new technology is to create structures that can change their shapes to attenuate vibrations and produce an increase in vehicle stability and performance [3, 4]. Recently, the application trend is oriented towards the implementation of such adaptive aerospace structures in the form of multitasking components to simultaneously reduce noise and vibrations, modify and control the wing shape, control the alignment accurately, conduct fault detection, etc. [3].

One of the most interesting areas of smart structure applications is the *morphing wing* aircraft, which changes its wings' shape over multiple and dissimilar

*Corresponding author: École de Technologie Supérieure, 1100 rue Notre-Dame Ouest, Montréal, Québec H3C 1K3, Canada.
email: ruxandra.botez@etsmtl.ca

flight segments as a function of flight conditions. The changes of the wing geometry and shape over different flight segments could maximize aircraft efficiency and performance for a complete flight. At the same time, it is very important to determine the advantages and the gains of a morphing wing aircraft versus a baseline un-morphed aircraft [1, 2].

Morphing wing refers to an aircraft wing that can change in size and shape during flight, thereby significantly modifying the aircraft's standard performance or characteristics. The morphing wing technology is not a totally new concept. Most aircraft wings already have components which allow the wing to change its shape (ailerons, flaps, etc.). The systems currently used in flight control might deflect the air flow in a desired direction, causing more lift by changing the airfoil camber. Also, for every existing (known) aircraft, there is a method for changing the wing configuration: folding, telescoping, sweeping, etc. The control of the wing surface is realized using different methods through the relative displacements of rigid structures [5]. On the other hand, numerical simulation of aircraft aerodynamics and experimental tests already show that aircraft performance would increase in many ways if the wing changes its shape and size, or twists to a desired configuration to achieve the appropriate conditions for flight control [3], compared to merely incorporating a flap to the wing. These changes would allow the wing to adapt itself to different flight conditions [6].

Many theoretical and experimental studies on morphing wings have been performed. These studies began with the work on independent airfoils and then extended to particular airplane configurations such as UAVs. A broad range of aerodynamic optimization strategies have been adopted for airplane design. In reference [7], the research study has focused on the shape of a morphing airfoil section and on the relative strain-energy needed to morph from one shape to another, which is considered as an additional design factor. The study was also focused on evaluating the drag design objective while constraints are enforced on the lift. In reference [5], the main objective of wing morphing was the increase of the aircraft efficiency to achieve the lowest fuel consumption during the landing phase, where the optimization criterion was the lift/drag ratio reduction. Aerodynamic morphing wing models were developed in reference [8] using Prandtl's Lifting Line Theory. A methodology was provided to compute the spanwise distribution of the vorticity on a finite wing. The results were expressed in terms of an extended operating envelope for the wing angle of attack. In reference [9], the overall project objective was to design, fabricate, integrate, and verify a wing demonstrator able to morph

its shape to increase lift for two distinct flight conditions in a wind tunnel test.

The benefits and the drawbacks of the morphing wing concept and practicality should be evaluated together. Aircrafts with morphing mechanisms will have additional weight and energy consumption owing to the power required by the actuators [2]. The mechanisms that would allow the morphing wing concept to be realized for a commercial or military aircraft have been impractical because of the weight and the cost effectiveness constraints. Smart materials have been useful, indeed, in the actuation and control systems for these types of hi-tech applications, such as Shape Memory Alloys (SMAs), and piezoelectric and magneto-strictive materials, but their deformation is controlled by their temperature which, in turn, is controlled by a supplied electrical current or magnetic field [6, 10–12]. Currently, these new smart material technologies have enabled research towards morphing wings concepts, while observing aerodynamic efficiency, cost, and weight constraints [13]. Specialists have estimated that the weight constraint might be removed and the morphing mechanism might be made more practical by using these advanced smart materials. However, these materials are still being evaluated and investigated, and the certification process required for their use in commercial and military aircraft with human pilots has not yet been fulfilled.

In order to achieve the optimal outcome from the aerodynamic studies, the actuation line of the morphing structure must be precisely controlled. Several control strategies have been adopted in different morphing applications as complex functions of the morphing structure and actuator types. In one case, the actuators were composed of stepper motors controlled with Chopper Drive Cards' separate circuit boards [14]. These drive cards use an external DC power source, and contain a timer to output pulses to the actuator stepper motor. By varying a potentiometer on the drive card, the step rate of the actuator can be varied, allowing its speed and force outputs to be controlled. Several robust control designs for a morphing airfoil concept are presented in reference [15]. An H_∞ controller and a two-degrees-of freedom H_∞ loop-shaping controller, that track the commanded lift and roll moments, respectively, were designed based on a linear aero-elastic model of a morphing wing. A control system was built for the SMA actuator operated airfoil [16]. A wing airfoil prototype was measured using optical fibre sensors and traditional strain gauges. External laser sensors were used to measure the displacements of the upper and lower surfaces and the trailing edge. Shape changes were obtained by embedding SMA

wire actuators into fibre-reinforced polymer composite structures. The SMA actuators were activated with Joule heating, and the temperature was measured with integrated thermocouples and optical fibre temperature sensors. An unsupervised learning simulation using the Q-Learning method was developed in references [17, 18] to learn about the optimal shape and shape change policies for a problem with four state variables. Optimality was addressed by rearward functions based on airfoil properties such as lift, drag, and moment coefficients. The reinforcement learning, as applied to morphing, was integrated on a computational airfoil model.

The objective of the research presented here is to develop an actuation control concept for a new morphing mechanism using smart materials such as SMA as actuators. These smart actuators deform the upper wing surface, made of a flexible skin, so that the laminar-to-turbulent transition point could move close to the wing trailing edge. The ultimate goal of this research project is to obtain a drag reduction as a function of flow condition by changing the wing shape. This research work was a part of a morphing wing project developed by the Ecole de Technologie Supérieure in Montréal, Canada, in collaboration with the Ecole Polytechnique in Montréal and the Institute for Aerospace Research at the National Research Council Canada (IAR-NRC).

A first phase of this project involved the determination of optimized airfoils available for 35 different flow conditions expressed in terms of five Mach numbers and seven angles of attack combinations. The optimized airfoils, derived from a laminar WTEA-TE1 reference airfoil [19, 20], were calculated and were used as a starting point in the actuation system design. Three steps were completed in the actuation system design phase: optimization of the number and positions of flexible skin actuation points, establishment of each actuation line's architecture, and the analytical modelling of the smart materials actuators used in this application. The next phase of the project is about the design of the actuation control, for which an integrated on-off versus PI architecture was chosen. In this design, numerical simulations of the open-loop morphing wing integrated system, based on a SMA non-linear analytical model, were performed. As subsequent validation methods, a bench test and a wind tunnel test were conducted.

This article is organized as follows. Section 2 briefly introduces the morphing wing system architecture and requirements. Section 3 describes the actuation lines' design and instrumentation. Section 4 presents how the integrated controller was designed. Section 5

presents the conclusions for the controller design phase.

2 MORPHING WING SYSTEM ARCHITECTURE

The final aim of our research project is the development of a morphing wing system that can delay the laminar-to-turbulent transition point close to the wing trailing edge. The transition location detection is based on pressure signals measured by optical and Kulite sensors installed on the upper wing flexible surface. Depending on the project evolution phase, two architectures are considered for the morphing system: open loop and closed loop. The difference between these two architectures is given by the use of the transition point as feedback signal.

The work described here was developed in the open-loop phase of the morphing wing system. In this phase, numerical and experimental studies were performed for the aerodynamics of the morphed wing, flexible skin structure, actuation hardware, and the actuation system control. Also, the studies include the real-time determination and visualization of the transition point position using the pressure sensor system and infrared camera visualization. The functions of the optical and Kulite pressure sensors are limited to the monitoring of the pressure and its root mean square distribution in the boundary layer.

The wing model has a rectangular plan form of 0.5 m chord and 0.9 m span. The wing airfoil cross-section is based on the reference airfoil WTEA-TE1. Part of the wing upper surface was covered by a flexible skin made of composite materials (layers of carbon and Kevlar fibres in a resin matrix) driven by two actuation lines (Fig. 1). Each actuation line uses SMA wires as actuators. At the same time, 32 pressure sensors (16 optical and 16 Kulite) were distributed on the flexible skin chordwise and spanwise as shown in Fig. 2. These sensors were positioned on two diagonal lines at an angle of 15° from the wing centre line. The rigid lower structure was made from aluminium alloy, and was designed to allow space for the instrumentation hardware and actuation system with its wiring.

The reference airfoil was optimized for 35 air flow cases. Therefore, 35 optimized morphing airfoils were obtained. The flow conditions were established as a combination of five Mach numbers (from 0.2 to 0.3 with an increment of 0.025) and seven incidence angles (from -1° to 2° with an increment of 0.5°). The Reynolds numbers (expressed in millions) for the previous five Mach number cases are: 2.29, 2.57, 2.84, 3.10, and 3.37. For each flow case, the transition point should be kept as close as possible to the trailing edge for the optimized airfoils. The flexible skin

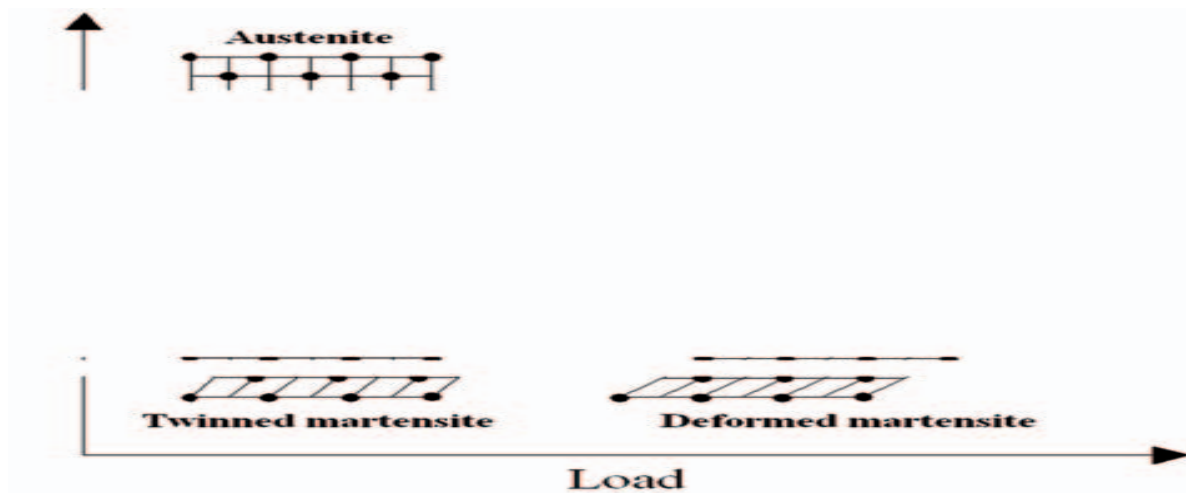


Fig. 1 General architecture of the mechanical model

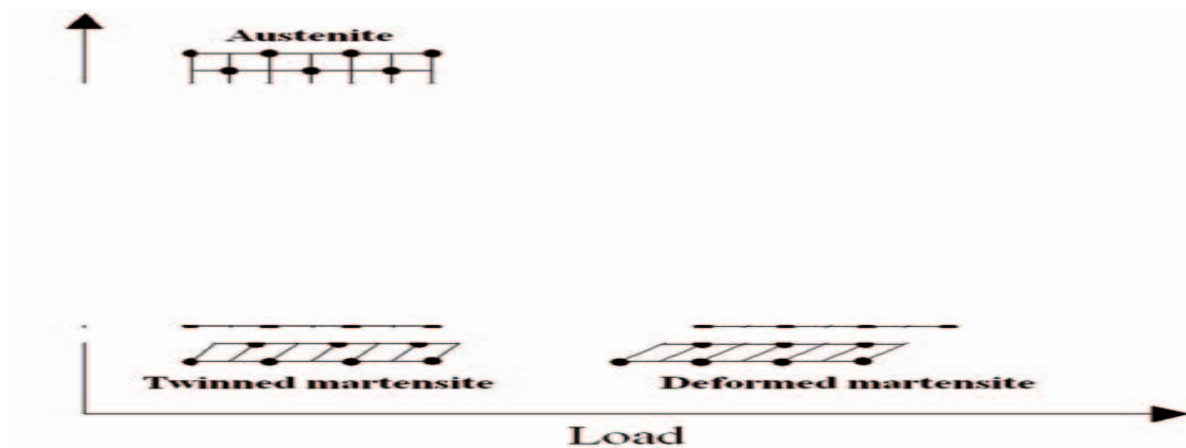


Fig. 2 Pressure sensor distribution on the flexible skin

spans the surface wing from 1 per cent to 70 per cent of the chord. Two actuation rods were incorporated at 25.3 per cent and 47.6 per cent of the chord, respectively.

3 ACTUATION MECHANISM CONCEPT

The shape memory actuator wires were made of nickel–titanium, and they contract as muscles do when electrically excited. This ability of stretching or shrinking is a characteristic of certain alloys that dynamically change their internal structure at a certain temperature. These alloys have the properties of exhibiting martensitic transformation when they deform at a low temperature phase, and may recover their original shape after heating [21]. This phase change, from martensite to austenite, is shown in Fig. 3 [9, 13]. The load changes the internal forces between the atoms, forcing them to change their

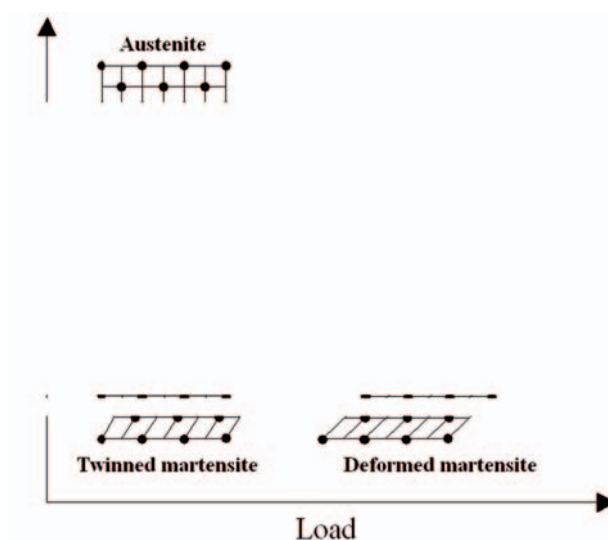


Fig. 3 SMA phase change

positions in the crystals and consequently forcing the wires to lengthen, which is called the SMA activation or the initial phase. When the wire is heated using a current, the heat generated by the current resistivity causes the atoms in the crystalline structure to realign and force the alloy to recover its original shape. Therefore, any change in the alloy's internal temperature would modify the crystalline structure accordingly and thus the wire's exterior shape. This property of changing the wire length as a function of the electrical current passing through the wire is used for actuation purposes [21]. Another major reason for the use of Nitinol and Ni-Ti material is that Nitinol is the most effective material at withstanding repeated cycles of heating and cooling without exhibiting any fatigue phenomenon [6].

SMA wires can execute the deflections resulting from contracting or expanding forces and can provide a variety of shapes and sizes that are extremely useful to achieve actuation system goals. For example, SMA wires can provide high forces corresponding to small strains to achieve the right balance between the forces and the deformations, as required by the actuation system. To ensure a stable system, a compromise or balance must be established and maintained. The structural components of the actuation system should be designed to respect the actuators' capabilities to accommodate the required deflections and forces.

Besides these numerous advantages, SMAs do have their disadvantages. They require a high electrical current to rapidly heat up to the transformation temperature. There are also surface-contact problems in their attachment to other structures. They maintain their volume during the entire transformation process; the decrease in length is accompanied by a diameter increase. The wire cannot be directly

welded or epoxied to a surface because, after several cycles of operation, the attachment would break down. Another issue, which reduces a wire's reliability, is over-heating or over-straining. If a wire is easily over-heated or over-strained, the number of cycles of operation will dwindle from thousands down to hundreds of times. Overall, the SMA actuator's disadvantages were deemed to be very small and manageable compared to the problems of the other types of smart actuators.

SMA wires as actuators can be used in several different ways. They can be used as straight wires, or they can be coiled to act as a spring, or they can be bent and used in a 'V' configuration [9]. The first choice is what was determined as the best option for the morphing wing application. Several criteria were incorporated, the primary being the desired deflection; however, the required forces were considerable. The actuation mechanism concept is shown in Fig. 4 [22] (the actuator image is displayed in Figs 1 and 2).

Each of our actuation line assemblies contains three SMA wires (1.8 m in length each) as actuators and a cam that is sliding spanwise on the supporting plate (on the x -axis as displayed in Fig. 4). The spanwise translating motion is translated into vertical displacement (z -direction) using rollers. A compression gas spring was also used as a recall. When the SMA is heated, the actuator contracts and the cam moves to the right and upwards pushing the flexible skin outwards. Cooling of the SMA results in a cam motion to the left and causes the skin to move inwards. The horizontal displacement is converted into a vertical displacement at a rate of 3:1, which gives the conversion of the horizontal stroke of x mm into a vertical stroke $z = x/3$ mm; then the cam factor is $c_f = 1/3$. From the optimized airfoil shapes, an approximate

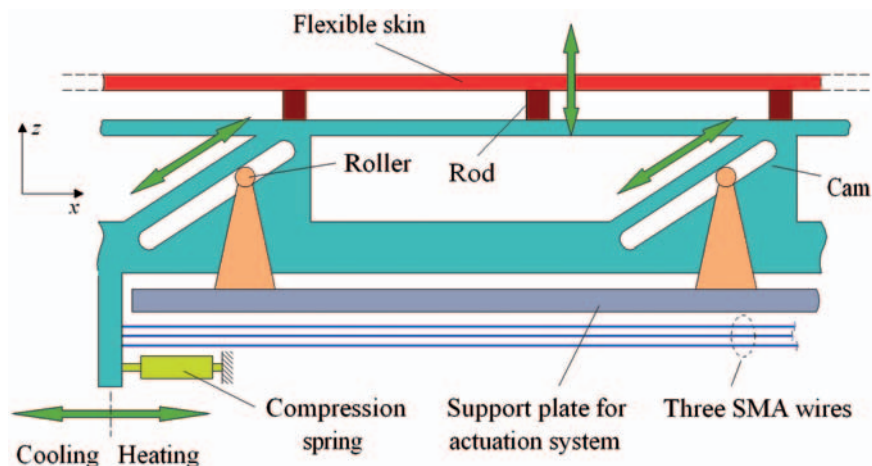


Fig. 4 The actuation mechanism concept

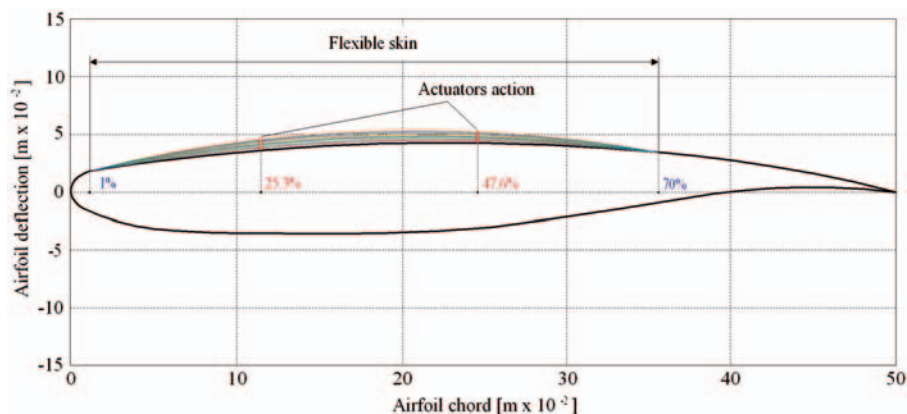


Fig. 5 Morphed airfoil shapes for different flow cases

value of 8 mm maximum vertical displacement was achieved for the rods (Fig. 5), which thus required a maximum horizontal displacement of 24 mm from the actuators.

4 ACTUATORS' INTEGRATED CONTROL DESIGN AND NUMERICAL SIMULATION

In this article, the design and testing of an SMA actuator controller is presented. The SMA actuator control can be achieved using any method for position control. However, the specific properties of SMA actuators such as hysteresis, the first cycle effect, and the impact of long-term changes must be considered. Starting from the established concept of the actuation system, the operating scheme of the controller can be developed, as illustrated in Fig. 6.

Based on the 35 studied flight conditions, a database of the 35 optimized airfoils was built. For each flight condition, a pair of optimal vertical deflections (dY_{1opt} , dY_{2opt}) for the two actuation lines is apparent. The SMA actuators morphed the airfoil until the vertical deflections of the two actuation lines (dY_{1real} , dY_{2real}) became equal to the required deflections (dY_{1opt} , dY_{2opt}). The vertical deflections of the real airfoil at the actuation points were measured using two position transducers. The controller's role is to send a command to supply an electrical current signal to the SMA actuators, based on the error signals (e) between the required vertical displacements and the obtained displacements. The designed controller was valid for both actuation lines, which are practically identical.

During the first phase of the controller design, numerical simulation of the controlled actuation system was performed; a step which required an SMA actuator model. In the literature, the modelling and control of smart material actuators can be

categorized as recent research fields. Technical literature is available in three independent domains: modelling, control, and smart materials. A smart actuator is formulated for a large range of smart materials and devices, and can be found in a variety of different configurations. It is common knowledge that all physical systems, including smart actuators, contain non-linearities. As a consequence, linear modelling of smart material actuators may contain errors, while non-linear modelling is possible.

The non-linear model used here is based on a numerical finite element method and was built by Terriault et al. [23] using Lickhatchev's theoretical model. The inputs of the SMA model are the alloy initial temperature, the electrical current (heating), and the applied force; the outputs are the actuator displacement and the alloy temperature. To use the SMA shape-changing characteristics, an initialization by an external force is required to pass initially through the transformation phase and then return to the initial phase at the end of the cooling phase. Owing to the intrinsic behaviour of the SMA [21, 23], the control could not be realized.

A wing can be regarded as a body moving in free air, where its molecules near the body are disturbed and displaced around to contain the wing. Owing to flow circulation, depending on the body shape, aerodynamic forces applied on the body are generated. The magnitudes of these forces depend on the wing dimensions and speed, and on the density and dynamic viscosity. The aerodynamic forces vary as a function of the airflow characteristics (Mach number, Reynolds number, and angle of attack). Since the aerodynamic pressure load on the flexible skin results in a significant suction, the SMA wire is shortened and the flexible wing skin is pulled outwards. Then, a gas spring is needed to counteract the aerodynamic forces, so that the resultant force acting on

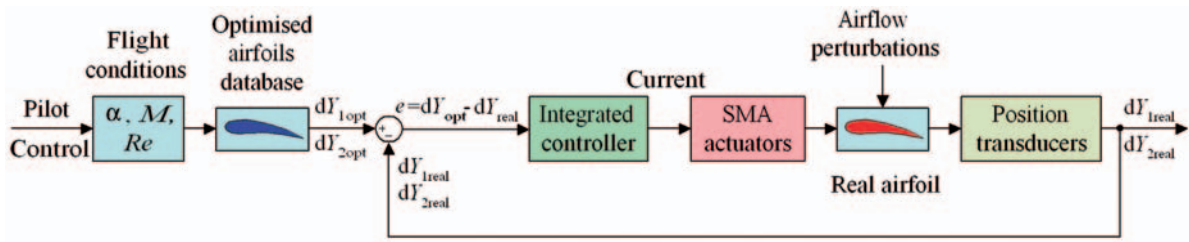


Fig. 6 Operating scheme of the SMA actuator control

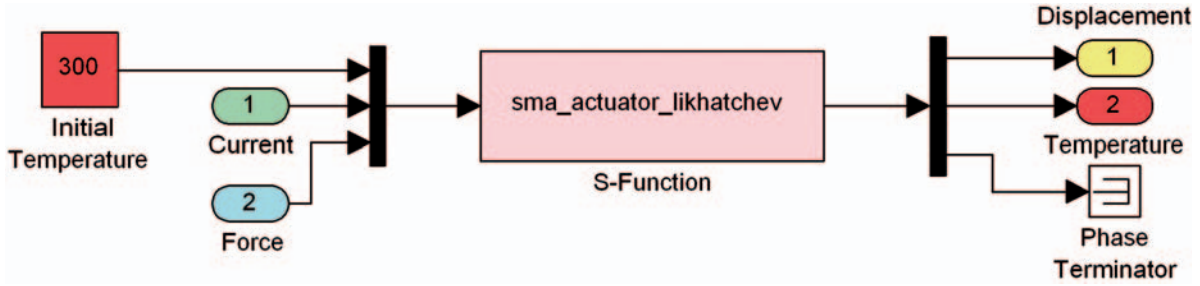


Fig. 7 The SMA S-function numerical model used in Simulink

the SMA wire can be calculated from the following equation

$$F_{SMA} = F_{spring} + (F_{skin} - F_{aero}) \cdot c_f \quad (1)$$

Initially, the SMA actuators are preloaded by the gas springs even when there is no aerodynamic load applied on the flexible skin. Then, equation (1) becomes

$$F_{SMA} = (F_{pretension} + k_{spring} \cdot \delta_h) + (k_{skin} \cdot \delta_v - F_{aero}) \cdot c_f \quad (2)$$

where

$$\begin{aligned} F_{spring} &= F_{pretension} + k_{spring} \cdot \delta_h \\ F_{skin} &= k_{skin} \cdot \delta_v \end{aligned} \quad (3)$$

where F_{SMA} is the resultant force acting on the SMA, F_{spring} the gas spring elastic force, F_{skin} the flexible skin elastic force, F_{aero} the aerodynamic force, $F_{pretension}$ the pretension force of the spring, and c_f is the cam factor. The parameters k_{spring} and k_{skin} are the spring and the skin elastic coefficients, respectively. The quantities δ_h and δ_v are the horizontal and vertical actuated displacements ($\delta_h/\delta_v = 3/1$), respectively.

The aerodynamic forces acting at the two actuation points on the flexible skin can be calculated by integrating the static pressure distribution δp over the flexible skin surface. Therefore, for the first actuator, one can obtain

$$F_{aero1} = \int_{(x_1+x_2)/2}^0 \delta p \cdot dx \quad (4)$$

while for the second one

$$F_{aero2} = \int_{0.7c}^{(x_1+x_2)/2} \delta p \cdot dx \quad (5)$$

where x_1 and x_2 are the actuators' chordwise positions. The pressure distribution p on the flexible skin can be deduced from the computed pressure coefficient C_p , while assuming that the pressure inside the wing box is equal to the tunnel static pressure p_∞ . The pressure coefficients for given Mach and Reynolds numbers and angle of attack are calculated using the Xfoil software

$$\delta p = p - p_\infty = \frac{1}{2} \rho_\infty V_\infty^2 \cdot C_p = Q_\infty \cdot C_p \quad (6)$$

where ρ_∞ is the free-stream air density, V_∞ the free-stream air speed, and Q_∞ the dynamic pressure.

The simulation model, shown in Fig. 8, was obtained by implementing the SMA actuator model using a Matlab S-function (Fig. 7). As can be observed from the figure, in order to control the SMA actuators, an adequate electrical current supply is required. The length of the SMA wires is a complex function of the SMA load forces and temperatures, and the latter is influenced by the supplying current over time and by the interaction of the wires with the environment in the cooling phase (when the electrical supply is off) [24].

The 'Mechanical system' block, illustrated in Fig. 8 with its scheme presented in Fig. 9, is modelled using equations (1) to (3). SMA actuators'

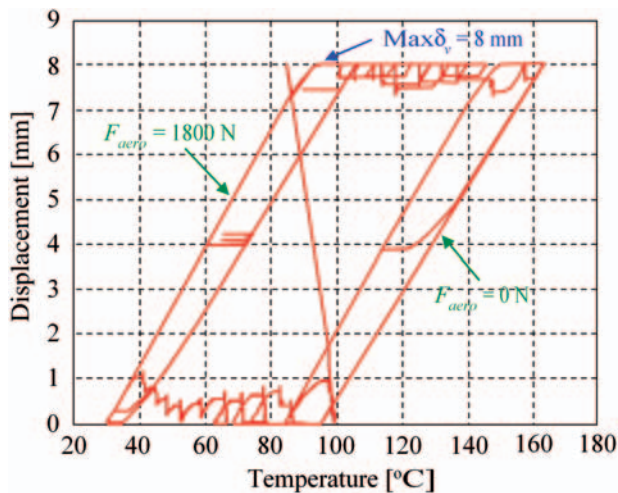


Fig. 10 SMA actuator simulated envelope

The envelope of the SMA actuator operability, obtained through numerical simulations for different aerodynamic load cases, is shown in Fig. 10, where the SMA initial wire length was equal to 1.8 m. As seen in Fig. 10, to obtain a maximum vertical displacement (8 mm) of the flexible skin, in the absence of aerodynamic forces, a current intensity corresponding to a temperature of approximately 162°C is needed to counteract the spring force. As the ability of the SMA wires to contract depends upon Joule heating to produce the required transformation temperature, the highest required temperature is the highest required electrical current. The required current and temperature values are decreased due to the reduction of the actuators' load by aerodynamic forces; i.e. for $F_{aero} = 1800$ N. Therefore, for the maximum vertical displacement, the required temperature is approximately 90°C. From another point of view, the ability of the SMA wires to return to their original state is dependent upon the ability of the system to cool the wires. The simulated SMA model offers summarized information on this subject, the proper heating and cooling of the wires being observed only during a thermodynamic analysis of the physical morphing wing. The architecture of the system plays an important role in cooling the wire by natural convection process. The wing model was designed to allow for natural cooling and heat evacuation from its top tip. The system performance can be negatively influenced by heat transfer from the actuators to the other wing components.

As shown in Fig. 6, the integrated controller's purpose is to control the SMA actuators by means of the electrical current supply, in order to cancel the distance deviation, e , between the required values for vertical displacements (corresponding to the

optimized airfoils) and the real values obtained from the position transducers. As mentioned previously, the design of such a controller is difficult due to the strong non-linearities of the SMA actuators' characteristics, non-linearities that are significantly influenced by the generated forces. The chosen design procedure consists of the following steps:

- Step 1: numerical simulation of the SMA model actuators for certain values of the forces in the system;
- Step 2: approximation with linear systems in the heating and cooling phases using Matlab's System Identification Toolbox and the numerical values obtained in Step 1;
- Step 3: choosing the controller type and its tuning for each of the two SMA actuator phases – heating and cooling;
- Step 4: integration of the two controllers just obtained into a single one, followed by its validation for the general model of the system (non-linear).

With the current established actuation line architecture ([22]), it is suggested that the pretension force of the gas spring must have the value $F_{pretension} = 1500$ N. Thus, $F_{aero} = 1500$ N value was chosen for the aerodynamic force in the numerical simulations. Simulating a cooling phase followed by a heating phase of the SMA actuators, using the model described in Fig. 8, the characteristics depicted were obtained (Fig. 11). The first graphic window of the figure presents the SMA wire length changing over time (δ_n), while the second one shows the SMA wire temperature values during two phases. A SMA wire dilatation occurs in the cooling phase, while a wire contraction is obtained in the heating phase. For a spanwise actuation distance of approximately 24 mm, the wire temperature reaches a value of 108°C. Note that the transient times to reach the steady-state values for the two phases are approximately 60 s for the cooling phase and approximately 40 s for the heating phase. For the steady state, after the cooling phase, the forces obtained by numerical simulation were: $F_{SMA} = 1000$ N, $F_{skin} = 0$ N, and $F_{spring} = 1500$ N. In this steady state, the system is not loaded and the vertical displacement of the actuator is null. After the cooling phase, the forces obtained by numerical simulation were: $F_{SMA} = 1337$ N, $F_{skin} = 266.1$ N, and $F_{spring} = 1571$ N. This steady state corresponds to the actuation system's maximal displacement, approximately 8 mm.

Using Matlab's System Identification Toolbox and the numerical values characterizing the response δ_n , at a series of successive step inputs, two transfer

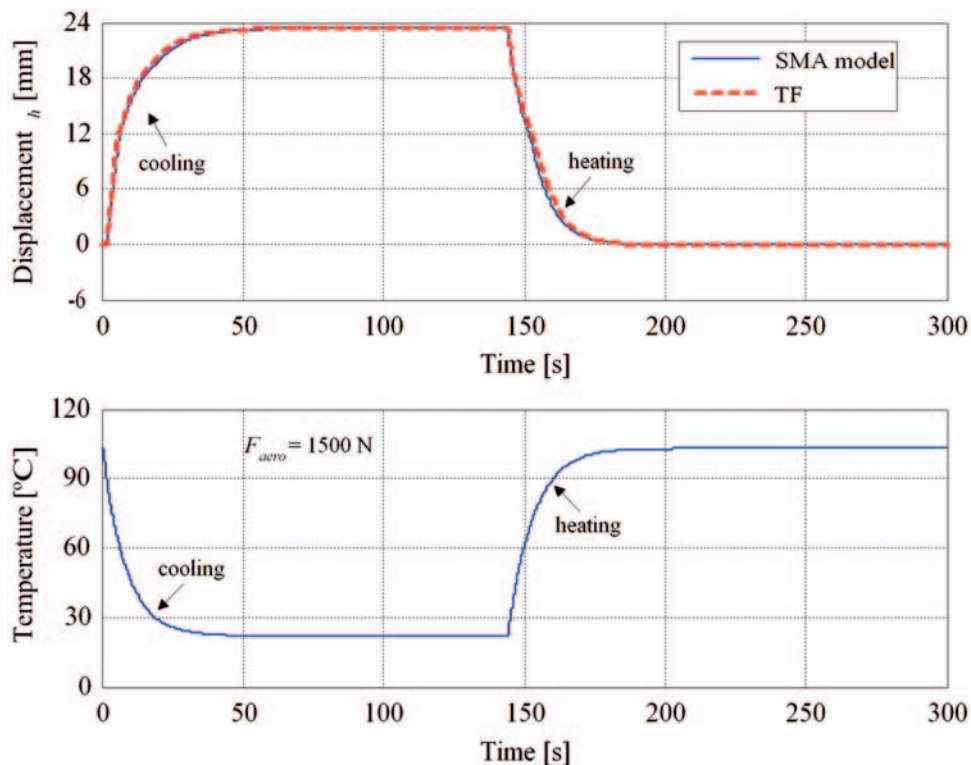


Fig. 11 Actuator displacement and temperature profile versus time (SMA model and corresponding transfer functions)

functions (TF) were found for the two SMA heating, $H_h(s)$, and cooling, $H_c(s)$, phases

$$\begin{aligned}
 H_h(s) &= \frac{1.77 \times 10^{-2}s^2 + 4.02 \times 10^{-3}s + 2.42 \times 10^{-2}}{s^3 - 1.44s^2 + 6.47 \times 10^{-1}s - 1.02 \times 10^{-3}}, \\
 H_c(s) &= \frac{3.54 \times 10^{-1}s + 2.67 \times 10^{-1}}{s^2 - 1.94s + 1.12 \times 10^{-2}}
 \end{aligned}
 \tag{7}$$

The displacements δ_n , corresponding to the linear systems obtained through the identification of the two phases, are depicted by the dashed-line in Fig. 11. A very good approximation can be observed for the two phases. The previously established transfer functions help to determine the controller type choice for each phase.

Since the SMA wire must be heated to contract and then cooled to dilate by providing an appropriate electrical current from the control block, it is normal that in the cooling phase the actuators are not powered. This phase of cooling may not only occur when controlling a long-term phase, when a change between two values of the actuator displacements is ordered, but also it can occur in a short-lived phase, where the real value of the deformation exceeds its desired value. However, it is imperative that in the heating phase the actuators are controlled

so that the stationary error of the automatic system goes to zero. Therefore, for this phase, a simpler PI type (proportional–integral) of architecture works best for the controller. It combines the advantages of a proportional-type controller, which substantially reduces the overshoot and leads to a short transient time, with the benefits of an integral controller, which cancels the steady-state system error. As a consequence, the PI controller must behave like a switch between the cooling and the heating phase, situations where the output current is 0 A, or is controlled by a PI-type law. The two phases’ interconnection leads to an integrated controller, which can be viewed as a combination of a bi-positional (particularly an on–off one) and a PI (proportional–integral) controller.

The input–output characteristic of a bi-positional (on–off) controller can be described by the equation

$$i(t) = \begin{cases} -i_m, & \text{if } e \leq 0 \\ i_m, & \text{if } e > 0 \end{cases}
 \tag{8}$$

where $i(t)$ is the command variable (electrical current) in time, i_m is the value of the command, and e the operating error (Fig. 6). The PI controller law is given by

$$i(t) = K_p \cdot e(t) + K_I \cdot \int e(t) \cdot dt
 \tag{9}$$

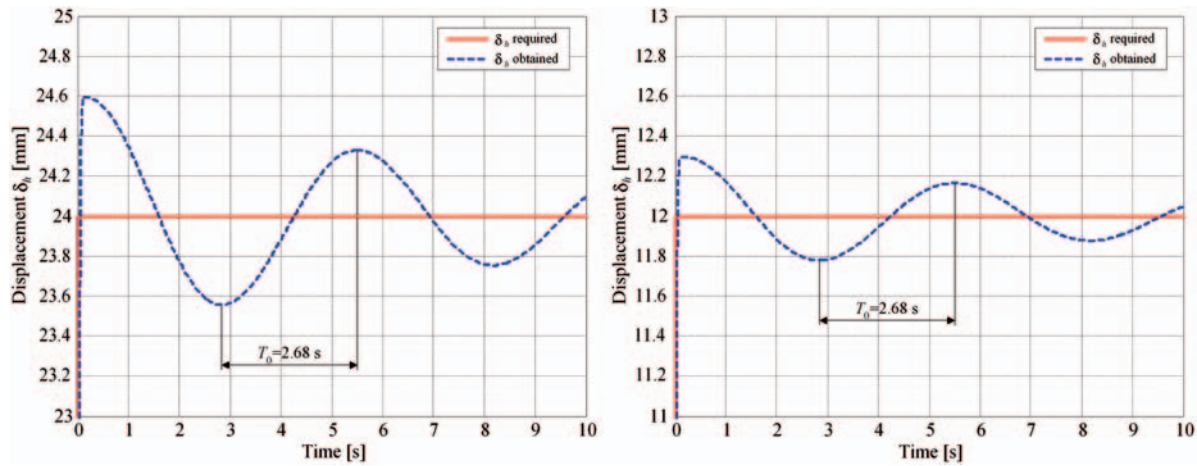


Fig. 12 The step input system responses for the proportional gain $K_{p0} = 3984$

where K_p is the proportional gain and K_I the integral gain. Combining the two controllers into one, based on the rules previously mentioned, the control law of the integrated controller becomes

$$\dot{i}(t) = \begin{cases} 0, & \text{if } e \leq 0 \\ K_p \cdot e(t) + K_I \cdot \int e(t) \cdot dt, & \text{if } e > 0 \end{cases} \quad (10)$$

The optimal tuning of the controller in the heating phase was realized using integral and minimum surface error criteria, known as the Ziegler–Nichols criterion [25]. Based on the minimization of the errors between the real and ideal responses of a system, the quality factor can be expressed in the form

$$I = \int_0^{\infty} (y_{\text{real}} - y_{\text{ideal}}) \cdot dt = \int_0^{\infty} \varepsilon \cdot dt = \min \quad (11)$$

where y_{real} represents the real output of the system, y_{ideal} its ideal output, and ε the difference between these two quantities. Taking the quality factor into account, Ziegler and Nichols proposed a tuning methodology for such controllers

Consider the regulator to be proportional (P) and that it is tuned with respect to the K_p parameter; Increase the amplification factor K_p until the response of the automatic system becomes self-sustained oscillatory. The value K_{p0} of K_p for which the system has an oscillatory behaviour with a semi-period (T_0) is recorded (equation (12)). The optimal values for the parameters of the PI regulator are determined using the following relations [25]

$$\begin{aligned} K_p &= 0.45 \cdot K_{p0} \\ K_I &= K_p / (0.85 \cdot T_0) \end{aligned} \quad (12)$$

Using the controller tuning methodology given above, the following numerical values for the PI controller parameters were obtained

$$\begin{aligned} K_{p0} &= 3984 \\ T_0 &= 2.68 \text{ s} \\ K_p &= 1792.8 \\ K_I &= 787.006 \text{ s}^{-1} \end{aligned} \quad (13)$$

The tuning values are also reflected by the step input system responses shown in Fig. 12 for the proportional gain $K_{p0} = 3984$.

With these values, the controlled system in the heating phase can be modelled with an approximate linear system with the block scheme described in Fig. 13.

The parameters $a_0 \div a_2$ and $b_0 \div b_3$ in the scheme are the coefficients of the $H_h(s)$ transfer function numerator and denominator in ascending powers of s (equation (7)). The open-loop transfer function of the controlled heating phase is then expressed in the form

$$H_{ol}(s) = C_{PI}(s) \cdot H_h(s) = \frac{q_3 s^3 + q_2 s^2 + q_1 s + q_0}{b_3 s^4 + b_2 s^3 + b_1 s^2 + b_0 s} \quad (14)$$

while the closed-loop transfer function is

$$H_{cl}(s) = C_{PI}(s) \cdot H_h(s) = \frac{q_3 s^3 + q_2 s^2 + q_1 s + q_0}{r_4 s^4 + r_3 s^3 + r_2 s^2 + r_1 s + r_0} \quad (15)$$

The coefficients are

$$\begin{aligned} q_3 &= K_p a_2 = 31.80 \\ q_2 &= K_p a_1 + K_I a_2 = 21.16 \\ q_1 &= K_p a_0 + K_I a_1 = 46.54 \\ q_0 &= K_I a_0 = 19.04 \end{aligned} \quad (16)$$

and

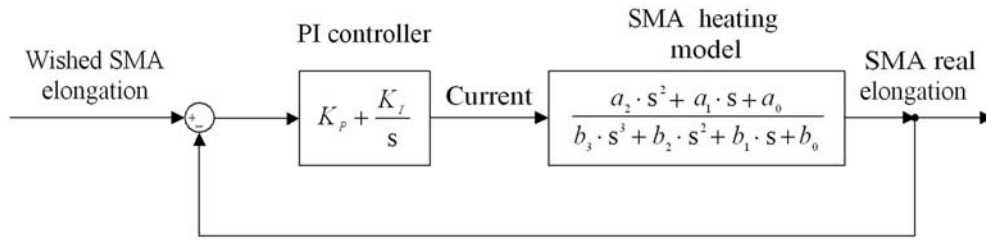


Fig. 13 The block scheme with transfer functions of the heating phase linear model

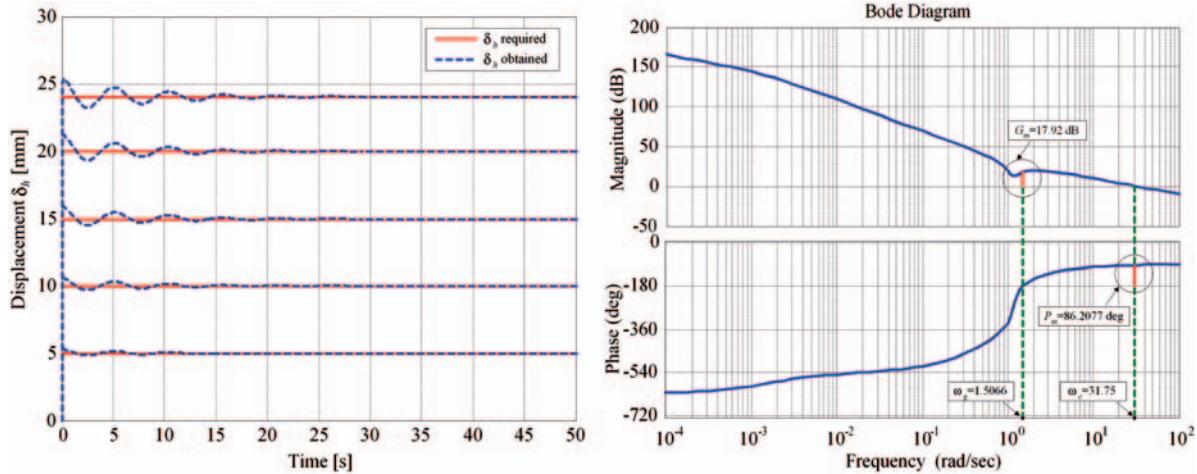


Fig. 14 The step input system response and the Bode diagram

$$\begin{aligned}
 r_4 &= b_3 = 1 \\
 r_3 &= b_2 + K_p a_2 = 30.36 \\
 r_2 &= b_1 + K_p a_1 + K_I a_2 = 21.81 \\
 r_1 &= b_0 + K_p a_0 + K_I a_1 = 46.54 \\
 r_0 &= K_I a_0 = 19.04
 \end{aligned}
 \tag{17}$$

$C_{PI}(s)$ is the transfer function of the PI controller. The poles of the closed-loop transfer function $H_{cl}(s)$ are realized with the values

$$\begin{aligned}
 p_1 &= -29.68, \quad p_1 \in \mathbf{R}_- \\
 p_2 &= -0.12 + 1.19 \cdot i, \quad p_2 \in \mathbf{C}, \text{Re}(p_2) \in \mathbf{R}_- \\
 p_3 &= -0.12 - 1.19 \cdot i, \quad p_3 \in \mathbf{C}, \text{Re}(p_3) \in \mathbf{R}_- \\
 p_4 &= -0.44, \quad p_4 \in \mathbf{R}_-
 \end{aligned}
 \tag{18}$$

It can be seen that all poles of the transfer function are placed in the left-hand side of the s -plane, and that the obtained system is stable. The system response for different step inputs and the Bode diagram starting from the $H_{ol}(s)$ transfer function are shown in Fig. 14. As can be seen, the stability of the system is confirmed, taking into account the values of both the gain margin (G_m) and the phase margin (P_m)

$$\begin{aligned}
 G_m &= 17.92 \text{ dB} = 0.13, \text{ associated frequency} \\
 \omega_g &= 1.51 \text{ rad/s} \\
 P_m &= 86.21^\circ, \text{ associated frequency} \\
 \omega_c &= 31.75 \text{ rad/s}
 \end{aligned}
 \tag{19}$$

In the state-space representation

$$\begin{aligned}
 \dot{\mathbf{x}}(t) &= \mathbf{A}\mathbf{x}(t) + \mathbf{B}u(t) \\
 \mathbf{y}(t) &= \mathbf{C}\mathbf{x}(t) + \mathbf{D}u(t)
 \end{aligned}
 \tag{20}$$

the state matrix \mathbf{A} , the input matrix \mathbf{B} , the output matrix \mathbf{C} and the feed-forward matrix \mathbf{D} were obtained by the forms

$$\begin{aligned}
 \mathbf{A} &= \begin{bmatrix} -30.36 & -21.81 & -46.54 & -19.04 \\ 1 & 0 & 0 & 0 \\ 0 & 1 & 0 & 0 \\ 0 & 0 & 1 & 0 \end{bmatrix}, \\
 \mathbf{B} &= \begin{bmatrix} 1 \\ 0 \\ 0 \\ 0 \end{bmatrix}, \quad \mathbf{C}^T = \begin{bmatrix} 31.80 \\ 21.16 \\ 46.54 \\ 19.04 \end{bmatrix}, \quad \mathbf{D} = 0.
 \end{aligned}
 \tag{21}$$

Evaluating the controllability and the observability matrix of the system (\mathbf{P} and \mathbf{Q} matrices) results in

$$\mathbf{P} = [\mathbf{B} \quad \mathbf{AB} \quad \mathbf{A}^2\mathbf{B} \quad \mathbf{A}^3\mathbf{B}]$$

$$= \begin{bmatrix} 1 & -30.36 & 900.30 & -26723.11 \\ 0 & 1 & -30.36 & 900.30 \\ 0 & 0 & 1 & -30.36 \\ 0 & 0 & 0 & 1 \end{bmatrix} \quad (22)$$

$$\mathbf{Q} = [\mathbf{C} \quad \mathbf{CA} \quad \mathbf{CA}^2 \quad \mathbf{CA}^3]^T$$

$$= \begin{bmatrix} 31.80 & 21.16 & 46.54 & 19.04 \\ -944.55 & -647.05 & -1460.98 & -605.58 \\ 28035.45 & 19139.32 & 43352.49 & 17986.36 \\ -832193.65 & -568090.67 & -1286744.78 & -533857.87 \end{bmatrix} \quad (23)$$

and

$$\text{rank}(\mathbf{P}) = \text{rank}(\mathbf{Q}) = \text{systemorder} = 4. \quad (24)$$

As a consequence, the system is completely controllable and observable, that is

for any initial state $\mathbf{x}(t_0) = \mathbf{x}_0$, there exists a function $\mathbf{u}(t)$ defined on a finite interval $(t_0, t_1]$, which independently brings the system into another state $\mathbf{x}(t_1) = \mathbf{x}_1$; and

matrices \mathbf{A} , \mathbf{C} and the output $\mathbf{y}(t)$, on a finite interval $(t_0, t_1]$, allow the determination of the state $\mathbf{x}(t_0) = \mathbf{x}_0$ of the system that has been started.

Taking into account the previous considerations, the final form of the integrated controller law is defined as follows

$$\dot{i}(t) = \begin{cases} 0, & \text{if } e \leq 0 \\ 1792.8 \cdot e(t) + 787 \cdot \int e(t) \cdot dt, & \text{if } e > 0 \end{cases} \quad (25)$$

5 CONCLUSIONS

The objective of this research was to develop an actuation control concept for a new morphing mechanism using smart materials, such as SMA, as actuators. These smart actuators modify the upper surface shape of a wing composed of a flexible skin so that the laminar-to-turbulent transition point moves close to the wing trailing edge. This technology can result in a substantial drag reduction. To achieve this aerodynamic goal, the first phase of the studies concerned the determination of some optimized airfoils for a number of flow conditions.

The designed controller controls the SMA actuators by means of the electrical current supply, with the objective of cancelling the deviation between

the required values for vertical displacements (corresponding to the optimized airfoils) and the real values (obtained from position transducers). The predicted envelope of the SMA actuator confirms that the length of the SMA wires is a complex function of the SMA load force and temperature. The flexible skin deformation is driven by a set of rollers and cam mechanisms, which are actuated by the SMA wires subject to controlled temperature; the SMA wires are contracted when heated and dilated when cooled. The heating phase is ensured by supplying a controlled electrical current and the cooling phase was passively realized by natural convection. A maximum vertical skin displacement (8 mm) can be achieved in the absence of aerodynamic force, but at high temperature in order to counteract the spring force.

One of the manageable inconveniences of the SMA wires' ability to contract is dependent upon Joule heating to produce the required transformation temperature, which is associated with high electrical current. Conveniently, the aerodynamic forces reduce the actuators' load; the required current and temperature values are decreased.

Starting from the strong non-linear SMA wire characteristics, the design procedure consisted of the following steps: (1) numerical simulation of the SMA model actuators for certain values of the forces in the system; (2) linear approximation of the system in the heating and cooling phases using the Matlab System Identification Toolbox and the numerical values obtained in the first step; (3) choosing and tuning of the controller type for each of the two SMA actuator phases; and (4) the integration of the two controllers obtained in step 3 into a single one.

It was found that the final configuration of the integrated controller is a combination of a bi-positional controller (on-off) and a PI (proportional-integral) controller, which behaved like a switch between the heating and cooling phases.

Using an integral criterion, the minimum error surface criterion (Ziegler-Nichols) and the PI controller for the heating phase, it was found that the system was optimally tuned and stable yielding tangible performance results.

After this preliminary design validation step described in this article 'part 1', a complete validation cycle of the 'on-off' and PI integrated controller was undertaken in part 2. The controller was realized numerically, on the real model for different values of the aerodynamic forces, and experimentally on a bench test with wind off and in the wind tunnel with wind on. That was performed for different actuation commands on the two actuation lines.

ACKNOWLEDGEMENTS

The authors thank the Consortium for Research and Innovation in Aerospace in Quebec (CRIAQ), Thales Avionics Inc., Bombardier Aerospace, and the National Sciences and Engineering Research Council (NSERC) for their financial support. The authors also thank Dr. George Henri Simon for initiating the CRIAQ 7.1 project and Dr. Philippe Molaret from Thales Avionics and Dr. Eric Laurendeau from Bombardier Aerospace for providing help and facilitating fruitful discussions.

© IMechE 2011

REFERENCES

- Smith, K., Butt, J., Spakovsky, M. R., and Moorhouse, D.** A study of the benefits of using morphing wing technology in fighter aircraft systems. In Proceedings of 39th AIAA Thermophysics Conference, Miami, Florida, USA, 25–28 June 2007.
- Butt, J. R.** A study of morphing wing effectiveness in fighter aircraft using energy analysis and global optimization techniques. MSc Thesis, Faculty of the Virginia Polytechnic Institute and State University, Blacksburg, Virginia, USA, December 2005.
- Hinshaw, T. L.** Analysis and design of a morphing wing tip using multicellular flexible matrix composite adaptive skins. MSc Thesis in Aerospace Engineering, Virginia Polytechnic Institute and State University, Blacksburg, Virginia, USA, 1 July 2009.
- Chopra, I.** Review of state of art of smart structures and integrated systems. *AIAA J.*, 2002, **40**(11), 2145–2187.
- Chang, P., Shah, A., and Singhee, M.** Parameterization of the geometry of a blended-wing-body morphing wing. Project report no. ME 6104, The Systems Realization Laboratory, Georgia Institute of Technology, Atlanta, Georgia, USA, 28 April 2009.
- Gonzalez, L.** Morphing wing using shape memory alloy: a concept proposal, final research paper in 2005 Summer Research Experience for Undergraduates (REU) on nanotechnology and materials systems. Texas Institute of Intelligent Bio-nano Materials and Structures for Aerospace Vehicles (TiiMS) – NASA Research University, Texas A&M University, July 2005, College Station, Texas, USA.
- Namgoong, H., Crossley, W. A., and Lyrintzis, A. S.** Aerodynamic optimization of a morphing airfoil using energy as an objective. In Proceedings of 44th AIAA Aerospace Sciences Meeting and Exhibit, Reno, Nevada, USA, 9–12 January 2006.
- Majji, M., Rediniotis, O. K., and Junkins, J. L.** Design of a morphing wing: modeling and experiments. In Proceedings of AIAA Atmospheric Flight Mechanics Conference and Exhibit, Hilton Head, South Carolina, USA, 20–23 August 2007.
- Baron, A., Benedict, B., Branchaw, N., Ostry, B., Pearsall, J., Perlman, G., and Selstrom, J.** Morphing wing (MoW), ASEN 4018 Senior Projects. Department of Aerospace Engineering, University of Colorado, Boulder, Colorado, USA, December 2003.
- Iannucci, L. and Fontanazza, A.** Design of morphing wing structures. In Proceedings of 3rd Systems Engineering for Autonomous Systems (SEAS) Defence Technology Centre (DTC) Technical Conference, Edinburgh, UK, 24–25 June 2008.
- Kota, S., Hetrick, J., Osborn, R., Paul, D., Pendleton, E., Flick, P., and Tilmann, C.** Design and application of compliant mechanisms for morphing aircraft structures. In Proceedings of SPIE—Smart Structures and Materials 2003: Industrial and Commercial Applications of Smart Structures Technologies, San Diego, California, USA, 3 March, 2003, pp. 24–33, Vol. 5054 (2003).
- Nickless, B. J.** Dynamic modeling and position control of a piezoelectric flexensional actuator. MSc Thesis, Graduate School of the University of Maryland, College Park, Maryland, USA, 2008.
- Thill, C., Etches, J., Bond, I., Potter, K., and Weaver, P.** Morphing skins. *Aeronaut. J.*, 2008, **112**(1129), 117–139.
- Bliss, T. K. and Bart-Smith, H.** Morphing structures technology and its application to flight control. In Proceedings of Student Research Conference, Virginia Space Grant Consortium Newport News, Virginia, USA, 1 April 2005.
- Whitmer, C. E. and Kelkar, A. G.** Robust control of a morphing airfoil structure. In Proceedings of American Control Conference, Portland, Oregon, USA, 8–10 June 2005.
- Ruotsalainen, P., Kroneld, P., Nevala, K., Brander, T., Lindroos, T., and Sippola, M.** Shape control of a FRP airfoil structure using SMA-actuators and optical fiber sensors. *J. Solid State Phenom.*, 2009, **144**—Mechatronic Systems and Materials II, 196–201.
- Lampton, A., Niksch, A., and Valasek, J.** Reinforcement learning of a morphing airfoil-policy and discrete learning analysis. In Proceedings of AIAA Guidance, Navigation and Control Conference and Exhibit, Honolulu, Hawaii, USA, 18–21 August 2008.
- Lampton, A., Niksch, A., and Valasek, J.** Morphing airfoils with four morphing parameters. In Proceedings of AIAA Guidance, Navigation and Control Conference and Exhibit, Honolulu, Hawaii, USA, 18–21 August 2008.
- Khalid, M. and Jones, D. J.** Navier stokes investigation of blunt trailing edge airfoils using O-grids. *AIAA J. Aircraft*, 1993, **30**(5), 797–800.
- Khalid, M. and Jones, D. J.** A CFD investigation of the blunt trailing edge airfoils in transonic flow. In Proceedings of Inaugural Conference of the CFD Society of Canada, CFD Society of Canada, Montreal, June 1993.
- Popov, A. V., Labib, M., Fays, J., and Botez, R. M.** Closed-loop control simulations on a morphing wing. *AIAA J. Aircraft*, 2008, **45**(5), 1794–1803.
- Georges, T., Brailovski, V., Morellon, E., Coutu, D., and Terriault, P.** Design of shape memory alloy

actuators for morphing laminar wing with flexible extradors. *J. Mech. Des.*, 2009, **31**(9), 091006.

23 Terriault, P., Viens, F., and Brailovski, V. Non-isothermal finite element modeling of a shape memory alloy actuator using ANSYS. *Comput. Mater. Sci.*, 2006, **36**(4), 397–410.

24 Grigorie, T. L. and Botez, R. M. Adaptive neuro-fuzzy inference system-based controllers for smart material actuator modeling. *Proc. IMechE, Part G: J. Aerospace Engineering*, 2009, **223**(6), 655–668.

25 Mihoc, D. *Teoria si Elementele Sitemelor de Reglare Automata*, 1980 (Editura Didactica si Pedagogica, Bucuresti).

APPENDIX

Notation

a_0 / a_2	coefficients of the $H_h(s)$ transfer function nominator	i_m	command value
A	state matrix	$i(t)$	command variable (electrical current)
b_0 / b_3	coefficients of the $H_h(s)$ transfer function denominator	I	quality factor
B	input matrix	k_{skin}	skin elastic coefficient
c	chord	k_{spring}	spring elastic coefficient
c_f	cam factor	K_I	integral gain
C	output matrix	K_P	proportional gain
C_p	pressure coefficient	K_{P0}	K_P value for which the system has an oscillatory behaviour
$C_{PI}(s)$	transfer function of the PI controller	LVDT	linear variable differential transducer
$dY_{1\text{opt}}$	optimal vertical displacement of actuator 1	M	Mach number
$dY_{2\text{opt}}$	optimal vertical displacement of actuator 2	p	pressure at the point where the pressure coefficient is evaluated
$dY_{1\text{real}}$	real vertical displacement of actuator 1	p_0 / p_4	poles of the closed-loop transfer function $H_{cl}(s)$
$dY_{2\text{real}}$	real vertical displacement of actuator 2	p_∞	pressure in the free-stream
D	feed-forward matrix	P	controllability matrix
e	actuation loop error	P_m	phase margin
F_{aero}	aerodynamic force	PI	proportional-integral
$F_{\text{pretension}}$	pretension spring force	q_0 / q_3	coefficients of the $H_{cl}(s)$ transfer function nominator
F_{skin}	elastic force produced by the flexible skin	Q	observability matrix
F_{spring}	elastic force of the gas spring	Q_∞	dynamic air pressure
F_{SMA}	resultant force that acts on the SMA	r_0 / r_4	coefficients of the $H_{cl}(s)$ transfer function denominator
G_m	gain margin	Re	Reynolds number
$H_c(s)$	identified transfer function for cooling phase	t	time
$H_{cl}(s)$	closed-loop transfer function of the controlled heating phase	T_0	oscillation semi-period
$H_h(s)$	identified transfer function for heating phase	TF	transfer function
$H_{ol}(s)$	open-loop transfer function of the controlled heating phase	$\mathbf{u}(t)$	command vector
		V_∞	free-stream velocity of the air
		x_1, x_2	actuator positions on the chord
		$\mathbf{x}(t)$	state vector
		y_{ideal}	ideal system output
		y_{real}	real system output
		$\mathbf{y}(t)$	output vector
		α	wing angle of attack
		δ_h, δ_v	horizontal and vertical actuated displacements
		δp	pressure distribution
		ε	difference between the ideal and the real system outputs
		ρ_∞	free-stream air density
		ω_c	frequency associated with the phase margin
		ω_g	frequency associated with the gain margin